Na$_x$MV(PO$_4$)$_3$ (M=Mn, Fe, Ni) Structure and Properties for Sodium Extraction

Weidong Zhou,[†] Leigang Xue,[†] Xujie Lü,[‡] Hongcai Gao,[†] Yutao Li,[†] Sen Xin,[†] Gengtao Fu,[†] Zhiming Cui,[†] Ye Zhu,[§]* John B. Goodenough[†]**

† Texas Materials Institute, The University of Texas at Austin, Austin, Texas 78712, United States
‡ Center for Integrated Nanotechnologies, Los Alamos National Laboratory, New Mexico, 87545, United States
§ Department of Applied Physics, The Hong Kong Polytechnic University, Hong Kong

* lytthu@gmail.com; ye.ap.zhu@polyu.edu.hk;

* jgoodenough@mail.utexas.edu

Keywords: sodium-ion batteries, cathode, NASICON, manganese, phosphates

The commercialization of large-scale rechargeable batteries for distributed stationary electric power storage and/or for powering electric road vehicles is projected to place too large demand on lithium deposits, since there is insufficient lithium available in the earth's crust if all the gas-engine-vehicle will be replaced with highly electrified vehicles. [1] Therefore, there is wide spread interest in the development of competitive sodium ions batteries, owing to the manifold abundance and low cost of Na, two hundreds time abundant of lithium in nature.[2-6] In a sodium battery, a critical component is the cathode materials. Three types of sodium-insertion components have been identified: layered oxide or sulfides,[7] cyano-perovskites[8] and framework oxides.[9] Among the framework structures, Na$_3$V$_2$(PO$_4$)$_3$ with the hexagonal NASICON (Na$^+$ super ionic conductor) type structure delivers the best electrochemical performance,[10][11] showing a highly reversible capacity of 110 mA h g^{-1} in a flat voltage plateau of 3.4 V associated with the V^{4+}/V^{3+} redox couple. The initial coulombic efficiency can reach as high as 97% with good cycling and rate performance owing to the fast Na$^+$ transfer in the crystal structure. Although Na$_3$V$_2$(PO$_4$)$_3$ shows promise in terms of applications, substitution of V with other lower cost and earth-abundant active elements remains essential

due to the relatively high cost of elemental V. Moreover, replacement of V allows for a possibility to improve the cell voltage.

Here, we report an investigation of the NASICON structures $Na_4MnV(PO_4)_3$ and $Na_3FeV(PO_4)_3$ as cathode materials for sodium-ion batteries. Both materials deliver an initial capacity of around 100 mAh g^{-1} and show stable capacities over 1000 cycles. $Na_4MnV(PO_4)_3$ exhibits two flat voltage plateaus located at about 3.6 V and 3.3 V, $Na_3FeV(PO_4)_3$ shows two voltage plateaus at 3.3 V and 2.5 V, both with good capacity retention at 10 C, enable the discovery of highly durable cathodes for sodium-ion batteries with cost-effective elements for large-scale energy storage applications.

$Na_4MnV(PO_4)_3$ and $Na_3FeV(PO_4)_3$ were synthesized by a sol-gel method with the presence of PEG-400 as surfactant followed by calcination/carbonization of the precursor at 650 °C in argon.[12] The scanning electron microscopy (SEM) image in Figure 1a and 1b shows that uniform worm-like nanoparticles in a diameter of 100 nm stack together with some inter-particle pores. In this nano-structure, the small particle size and inter-particle void space facilitate ionic transfer in thicker electrode films and higher current density. The in-situ forming of carbon coating or carbon particles among the cathode particles improves the electrical conductivity since the transition metal phosphates usually suffer from low electrical conductivity as cathode materials.

Figure 1

High-resolution scanning transmission electron microscopy (STEM) images taken with an annular dark-field detector (ADF), Figure 1c and 1d, show that both $Na_4MnV(PO_4)_3$ and $Na_3FeV(PO_4)_3$ have an ordered single-phase crystal structure and the particles maintain this structure all the way to the surface. Electron energy loss spectroscopy (EELS) show strong signals of Mn, V, O and Fe, V, O, validating the composition of $Na_4MnV(PO_4)_3$ and $Na_3FeV(PO_4)_3$ (Figure 1e and 1f), respectively. The thermogravimetric analyses (TGA) of

both $Na_4MnV(PO_4)_3$ and $Na_3FeV(PO_4)_3$ show that around 7~8% carbon is contained in the synthesized samples <mark>Figure S</mark>1.

Figure 2

Rietveld analysis of the X-ray diffraction (XRD) pattern confirmed the existence of a pure single phase (in Figure 2), with similar lattice parameters as those obtained from single-crystal analysis. The lattice parameters obtained for the $Na_4MnV(PO_4)_3$ nanoparticles were a=8.9622 Å and c=21.5061 Å with a R3-c trigonal structure; these values compare well with existing structure of $Na_4Fe^{2+}Fe^{3+}(PO_4)_3$.[13] $Na_4MnV(PO_4)_3$ units comprise corner-shared Mn/VO_6 octahedral and PO_4 tetrahedral units to establish the anion framework $[MnV(PO_4)_3]^{4-}$. Two types of independent Na cations are located in the interstitial space of the framework with different oxygen environments, including six-fold coordination (Na_1) and ten-fold coordination (Na_2);[14] a facile two-dimensional Na^+ migration and a limited Na^+ transport in the third dimension has been determined. Due to a stronger bond force between O and Na at Na_1 sites, the ions at the Na_2 site are more easily extracted and inserted in the electrochemical redox process of energy storage. The structure of $Na_3FeV(PO_4)_3$ is a little different from that of the $Na_4MnV(PO_4)_3$, although Na cations in both are located in two different interstitial positions of the framework with multi-dimensional Na^+ migration pathways. In $Na_3FeV(PO_4)_3$, a cooperative distortion of the FeO_6 octahedron distorts the crystal structure to monoclinic.[15]

Figure 3

Aberration-corrected STEM was employed to obtain a direct vision of the atomic structure of $Na_4MnV(PO_4)_3$ for a better understanding of the sodium insertion mechanism, as shown in Figure 3 and <mark>Figure S</mark>2. Various projections, including [-111], [210], [001], [110], [5-21] and [48-1], were adopted for observation, because separated columns of Na, P, O and Mn/V ions are aligned in different crystal graphic directions and the atomic displacements are easily missed in a single direction.[16] As Mn and V share an identical position in $Na_4MnV(PO_4)_3$,

they are nearly indistinguishable in STEM images. The intensity of ADF-STEM images is sensitive to the atomic number and therefore the image contrast is dominated by heavy elements (Mn/V and P). The contrast of Na and O in ADF-STEM is much weaker and not clearly discernible in most projections, owing to the relatively low atomic number. The only exception is at the [210] zone axis where the Na-O columns show up next to the P columns (Figure 3c and 3d). All imaged atomic structure matches well with that for the NASICON lattice, where the Mn^{2+}/V^{3+} ions occupy the octahedral sites forming Mn/VO_6 octahedra and two types of Na^+ ions are surrounded by different oxygen coordination. The overall structure forms a trigonal lattice; Mn/V, Na_1 and Na_2 occupying, respectively, all the 12C, 6b and 18e sites. More projected lattice images along other directions ([001], [110] and [42-1]) in $Na_4MnV(PO_4)_3$ are shown in Figure S2, where an individual Mn/V surrounded by six PO_4 at a regular hexagon can be observed in [001] projection. Furthermore, the framework structure with void space in the atomic alignment for sodium migration can be clearly observed along [-111], [210], [5-21] and [48-1] directions in Figure 3. It creates Na-ion transportation channels with the dimension larger than that of the Na^+, which allows the fast transport of Na^+ in these channels.

Figure 4

Figures 4a and 4b are aberration-corrected ADF-STEM images of $Na_3VFe(PO_4)_3$. Compared with projected crystal structure of $Na_3V_2(PO_4)_3$ with space group R-3c and $Na_3Fe_2(PO_4)_3$ with C12c1,[17] as shown in Figure 4c-f, the STEM images of $Na_3VFe(PO_4)_3$ show a better match to that of the $Na_3Fe_2(PO_4)_3$ in Figure 4d and 4f in [001] and [101] projections. The other two STEM images also match well with the $Na_3Fe_2(PO_4)_3$ in [201] and [103] projections (Figure S3), further demonstrating that the $Na_3VFe(PO_4)_3$ adopts a monoclinic phase in good agreement with the results of XRD refinements in Figure 2. It is interesting that although Fe^{3+} and V^{3+} have similar dimension of 0.64~0.65 A, the $Na_3V_2(PO_4)_3$ adopts a R-3c structure while $Na_3Fe_2(PO_4)_3$ adopts a C12c1 structure. Meanwhile, the $Na_3VFe(PO_4)_3$ takes the same

monoclinic structure as $Na_3Fe_2(PO_4)_3$. It would appear that the combination of a Fe^{3+} ion and a Na3 sodium content stabilizes the monoclinic distortion to occur above room temperature.

Figure 5

Electrodes prepared from this material were examined in coin-type half-cells, with lithium metal as a counter electrode. The electrochemical behaviors of two materials were first determined by cyclic voltammetry (CV) scans, Figures 5a and 5b. Both $Na_4MnV(PO_4)_3$ and $Na_3FeV(PO_4)_3$ show two redox couples, which could be assigned to the multistep reduction mechanism of the different transition metals. According to the previously reported results, the redox peaks centered at about 3.6-3.5 V, 3.4-3.2 V and 2.7-2.4 V can be attributed to the equilibrium voltage of the Mn^{3+}/Mn^{2+}, V^{4+}/V^{3+} and Fe^{3+}/Fe^{2+} redox couple,[10],[18] respectively. Highly in agreement with the CV data, two well-defined charge/discharge plateaus were observed in both $Na_4MnV(PO_4)_3$ and $Na_3FeV(PO_4)_3$ (in Figure 5c and 5d). The $Na_4MnV(PO_4)_3$ delivers a capacity around 101 mAh g^{-1} at 1 C with two charge/discharge plateau at 3.6 V and 3.3 V, associated with the redox behavior of Mn^{3+}/Mn^{2+} and V^{4+}/V^{3+}. $Na_3FeV(PO_4)_3$ gives a capacity around 103 mAh g^{-1} at 1 C with two charge/discharge plateau at 3.3 V and 2.5 V, corresponding to the redox behavior of V^{4+}/V^{3+} and Fe^{3+}/Fe^{2+}. Neither the $Na_4MnV(PO_4)_3$ nor the $Na_3FeV(PO_4)_3$ electrodes experienced obvious capacity lost as the c-rate was increased from 1C to 10C (from101 mAh g^{-1} to 90 mAh g^{-1}), demonstrating excellent rate performance, which can be attributed to the uniform nano-size particle dimensions with porous morphology and high speed Na^+ migration in the NASICON framework structure.[19] Both compounds show a high initial coulombic efficiency of around 96-97% followed by a stable coulombic efficiency around 99%, suggesting low initial sodium consume in the cathode area, which is a benefit for the real application as commercial batteries since there is no excess sodium source in the full cells. In longer cycling at 1C, stable discharge capacities were observed for both structures, as shown in Figure 5e. After 1000 cycles, capacities of 90 mAh g^{-1} and 100 mAh g^{-1} were obtained for $Na_4MnV(PO_4)_3$ and $Na_3FeV(PO_4)_3$, respectively,

corresponding to the capacity retentions of around 89% and 95%. Generally, the manganese-based polyanion compounds typically suffer from some structural distortion in high oxidation state because of the appearance of Jahn-Teller active Mn^{3+}.[20] The good long-term cycling performance of $Na_4MnV(PO_4)_3$ indicates the presence of V^{4+} suppresses the cooperative geometric distortion and ensures the structural stability of the $Na_4MnV(PO_4)_3$ framework during long term extraction and insertion of sodium ions.

Figure 6

To reveal the structural change of the $Na_4MnV(PO_4)_3$ and $Na_3FeV(PO_4)_3$ cathodes during the extraction and insertion of sodium-ions, ex-situ XRD patterns were obtained at different depth of first charging and discharging process and are plotted in Figures 6a-6d. On the whole, growth of new peaks and simultaneous decrease of existing peaks were clearly observed throughout the entire first cycle. The peak at $2\theta=31-32°$ for both cathodes disappeared completely when charge to 3.8V and recovered gradually during discharge process. The peak at $2\theta=35-36°$ experienced obvious right-left shift continuously in the charge-discharge process, which is consistent with a change of crystal lattices when the transition metal in octahedral MO_6 is oxidized/reduced, accompanied with sodium ion extraction/insertion. In addition, some peaks experience peak merging or splitting, and then recover their original shapes after a full cycle. These above phenomena are typically observed in two-phase reactions and suggests that both $Na_4MnV(PO_4)_3$ and $Na_3FeV(PO_4)_3$ undergo successive biphasic transitions through various intermediate phases with preserving the overall framework,[21] which is consistent with the two well-defined charge-discharge voltage plateaus and superior electrochemical stability.

X-ray photoelectron spectroscopy (XPS) studies were carried out to examine the oxidation states of manganese and vanadium in $Na_4MnV(PO_4)_3$ at different charging states (Figure S4). The charge process is expected to be accompanied by the oxidation of vanadium from V^{3+} to V^{4+} and then manganese from Mn^{2+} to Mn^{3+}. Upon charge to 3.5 V, the binding energy of V

increased from 523.8 eV to 525.1 eV and the peak of Mn 2p does not show any obvious shift in this state, indicating the formation of a higher oxidation state only of V.[10] After further charge to 3.8 V, the binding energy of Mn $2p^{3/2}$ increased to about 642.8 eV from 641.9 eV, indicating the formation of Mn^{3+}.[22] These results show the successive bi-step extraction of two Na^+ ions from the $Na_4MnV(PO_4)_3$ accompanied by the successive oxidation of V^{3+}/V^{4+} and Mn^{2+}/Mn^{3+} to achieve the close-to-theoretical capacity.

To investigate further these bi-metal containing phosphates, $Na_4NiV(PO_4)_3$ was prepared through a similar method; but a pure NASICON phase was not obtained after many tries, which may be because some Ni take the position of Na and/or the formation of some pyrophosphate during the heat treatment.[23] In a half cell, $Na_4NiV(PO_4)_3$ shows an oblique one voltage plateau from 3.9 V to 3.3 V with capacities around 80 mAh g^{-1} at 1C and 70 mAh g^{-1} at 5C, indicating more than one sodium ions could be reversibly extracted. After 500 cycles, a capacity of 67 mAh g^{-1} at 5C was retained, around 83% of initial capacity, indicating a stable structure during long term sodium extraction-insertion cycling. The ex-situ XPS spectra show that the bonding energy of V increased and the bonding energy of Ni didn't change when charges to 3.5 V, corresponding to the exclusive oxidation of V^{3+}/V^{4+} at this stage.[24] Interestingly, the bonding energy of both V and Ni slightly increased after charge to 4.0 V, meaning both V and Ni were oxidized during the charge process. Since less than two sodium can be extracted in $Na_4NiV(PO_4)_3$, the Ni^{2+} and V^{4+} were both partially oxidized to Ni^{3+} and V^{5+} during charge from 3.5 V to 4.0 V.

In conclusion, we prepared three sodium ion battery cathode materials that not only show superior capacity and initial efficiency, but also have good durability and rate performance needed for commercial applications demanding. In $Na_4MnV(PO_4)_3$, the introduction of Mn lowers the cost of materials and improves the voltage compared with the $Na_3V_2(PO_4)_3$; the presence of V suppresses the geometric distortion of Mn^{3+} during charge and stabilizes the structure over long cycling. Therefore, the combination of Mn and V integrates the benefits

from each and addresses the problems of each. In addition, these materials exhibit two-dimensional ion conduction paths for facile sodium ion diffusion and, coupled with the nano-sized morphology, are capable of charge and discharge in a matter of minutes. Compared with the lithium ions batteries presently ubiquitous, these offer promising alternative due to the advantages in cost and wide availability of sodium.

Experimental Section

$Na_4MnV(PO_4)_3$ preparation: The starting precursors of sodium acetate, manganese acetate, vanadium acetylacetonate and phosphoric acid were dissolved in ethanol in the molar ratio 4 : 1 : 1 : 3 (Na : Mn : V : P) and stirred for 2 hours in the presence of PEG-400 (1%, V/V), followed by an evaporation of solvent. Subsequently, the as-prepared powder was annealed at 700 °C for 5 h under argon atmosphere to obtain the carbon mixed network of $Na_4MnV(PO_4)_3$.

Electrochemical analysis: The cathode sample, super P conductive carbon and CMC binder at a weight ratio of 75 : 20 : 5 were mixed in water to make the slurry for cathode film. Sodium metal, 1 M $NaClO_4$ in propylene carbonate (PC)/fluoroethylene carbonate (FEC) (10 : 1 v/v), and a glass fiber were used as the anode, electrolyte, and separator for the Na-ion half-cells, respectively.

STEM imaging and EELS: STEM observation was performed on a double-aberration-corrected FEI Titan[3] 80-300 FEG-TEM/STEM operating at 300 kV at Monash Centre for Electron Microscopy, Monash University. ADF-STEM images were acquired with a convergence semiangle of 21 mrad and an ADF inner collection angle 29 mrad. EEL spectra were acquired with a Gatan Image Filter (GIF) Tridiem Model 863 P using a 2mm entrance aperture (15 mrad collection angle). Both $Na_4MnV(PO_4)_3$ and $Na_3FeV(PO_4)_3$ materials are easy to be damaged under high-energy electron irradiation. Therefore STEM image and EELS are only carried out over fresh sample regions to avoid potential artefacts.

Supporting Information
Supporting Information is available online from the Wiley Online Library or from the author.

[1]   J. M. Tarascon, *Nat. Chem.* **2010**, *2*, 510.

[2]   V. Palomares, P. Serras, I. Villaluenga, K. B. Hueso, J. Carretero-Gonzalez, T. Rojo, *Energy Environ. Sci.* **2012**, *5*, 5884−5901.

[3]   a) M. D. Slater, D. Kim, E. Lee, C. S. Johnson, *Adv. Funct. Mater.* **2013**, *23*, 947–958; b) X. Xiang, K. Zhang, J. Chen, *Adv. Mater.* **2015**, *27*, 5343–5364.

[4]   H. L. Pan, Y. S. Hu, L. Q. Chen, *Energy Environ. Sci.* **2013**, *6*, 2338−2360.

[5]   D. Kundu, E. Talaie, V. Duffort, L. F. Nazar, *Angew. Chem. Int. Ed.* **2015**, *54*, 3431–3448.

[6]   S. W. Kim, D. H. Seo, X. H. Ma, G. Ceder, K. Kang, *Adv. Energy Mater.* **2012**, *2*, 710−721.

[7]   a) N. Yabuuchi, M. Kajiyama, J. Iwatate, H. Nishikawa, S. Hitomi, R. Okuyama, R. Usui, Y. Yamada, S. Komaba, *Nat. Mater.* **2012**, *11*, 512–517; b) D. Yuan, X. Liang, L. Wu, Y. Cao, X. Ai, J. Feng, H. Yang, *Adv. Mater.* **2014**, *26*, 6301–6306; c) S. Guo, P. Liu, H. Yu, Y. Zhu, M. Chen, M. Ishida, H. Zhou, *Angew. Chem. Int. Ed.* **2014**, *53*, 8963–8969.

[8]   a) Y. Lu, L. Wang, J. Cheng, J. B. Goodenough, *Chem. Commun.* **2012**, *48*, 6544–6546; b) J. Song, L. Wang, Y. Lu, J. Liu, B. Guo, P. Xiao, J.-J. Lee, X.-Q. Yang, G. Henkelman, J. B. Goodenough, *J. Am. Chem. Soc.* **2015**, *137*, 2658−2664.

[9]   a) P. Barpanda, G. Oyama, S. Nishimura, S. C. Chung, A. Yamada, *Nat. Commun.* **2014**, *5*, 4358; b) B. L. Ellis, W. R. M. Makhanouk, Y. Makimura, K. Toughilland, L. F. Nazar, *Nat. Mater.* 2007, 6, 749–753.

[10]   a) K. Saravanan, C. W. Mason, A. Rudola, K. H. Wong, P. Balaya, *Adv. Energy Mater.* **2013**, *3*, 444–450; b) Z. Jian, W. Han, X. Lu, H. Yang, Y.-S. Hu, J. Zhou, Z. Zhou, J. Li, W. Chen, D. Chen, L, Chen, *Adv. Energy Mater.* **2013**, *3*, 156–160; c) S. Li, Y. Dong, L. Xu, X. Xu, L. He, L. Mai, *Adv. Mater.* **2014**, *26*, 3545–3553.

[11]   a) J. B. Goodenough, H. Y. P. Hong, J. A. Kafalas, *Mater. Res. Bull.* **1976**, *11*, 203; b) C. Masquelier, A. K. Padhi, K. S. Nanjundaswamy, J. B. Goodenough, *J. Solid State Chem.* **1998**, *135*, 228.

[12]   J. Kang, S. Baek, V. Mathew, J. Gim, J. Song, H. Park, E. Chae, A. K. Rai, J. Kim, *J. Mater. Chem.* **2012**, *22*, 20857–20860.

[13]   F. Hatert, *Acta Crystallogr. Sect. E.* **2009**, *65*, i30.

[14]   W. Song, X. Cao, Z. Wu, J. Chen, K. Huangfu, X. Wang, Y. Huang, X. Ji, *Phys. Chem. Chem. Phys.* **2014**, *16*, 17681–17687.

[15]   A. S. Andersson, B. Kalska, P. Eyob, D. Aernout, L. Haggstrom, J. O. Thomas, *Solid State Ionics* **2001**, *140*, 63–70.

[16]   a) Z. Jian, C. Yuan, W. Han, X. Lu, L. Gu, X. Xi, Y.-S. Hu, H. Li, W. Chen, D. Chen, Y. Ikuhara, L. Chen, *Adv. Funct. Mater.* **2014**, *24*, 4265–4272; b) Y. Sun, L. Zhao, H. Pan, X. Lu, L. Gu, Y.-S. Hu, H. Li, M. Armand, Y. Ikuhara, L. Chen, X. Huang, *Nat. Commun.* **2012**, *4*, 1870; c) S. Guo, P. Liu, H. Yu, Y. Zhu, M. Chen, M. Ishida, H. Zhou, *Angew. Chem. Int. Ed.* **2015**, *54*, 5894–5899; d) P.-F. Wang, Y. You, Y.-X. Yin, Y.-S. Wang, L.-J. Wan, L. Gu, Y.-G. Guo, *Angew. Chem. Int. Ed.* **2016**, *55*, 7445 –7449.

[17]   C. Masquelier, C. Wurm, J. Rodríguez-Carvajal, J. Gaubicher, L. Nazar, *Chem. Mater.* **2000**, *12*, 525–532.

[18]   a) P. Barpanda, T. Ye, M. Avdeev, S.-C. Chung, A. Yamada, *J. Mater. Chem. A* **2013**, *1*, 4194–4197; b) P. Barpanda, G. Liu, C. D. Ling, M. Tamaru, M. Avdeev, S.-C. Chung, Y. Yamada, A. Yamada, *Chem. Mater.* **2013**, *25*, 3480−3487; c) P. Moreau, D. Guyomard, J. Gaubicher, F. Boucher, *Chem. Mater.* **2010**, *22*, 4126–4128.

[19]   a) C. Zhu, P. Kopold, P. A. van Aken, J. Maier, Y. Yu, *Adv. Mater.* **2016**, *28*, 2409–

2416; b) X. Rui, W. Sun, C. Wu, Y. Yu, Q. Yan, *Adv. Mater.* **2015**, *27*, 6670–6676.

[20]   J. B. Goodenough, Y. Kim, *Chem. Mat.* **2010**, *22*, 587–603.

[21]   R. A. Shakoor, D.-H. Seo, H. Kim, Y.-U. Park, J. Kim, S.-W. Kim, H. Gwon, S. Lee,

K. Kang, *J. Mater. Chem.* **2012**, *22*, 20535–20541.

[22]   J. C. Carver, G. K. Schweitzer, T. A. Carlson, *J. Chem. Phys.* **1972**, *57*, 973–982.

[23]   H. Kim, R. A. Shakoor, C. Park, S. Y. Lim, J.-S. Kim, Y. N. Jo, W. Cho, K. Miyasaka,

R. Kahraman, Y. Jung, J. W. Choi, *Adv. Funct. Mater.* **2013**, *23*, 1147–1155.

[24]   Y. Nanba, T. Iwao, B. M. Boisse, W. Zhao, E. Hosono, D. Asakura, H. Niwa, H.

Kiuchi, J. Miyawaki, Y. Harada, M. Okubo, A. Yamada, *Chem. Mater.* **2016**, *28*, 1058–1065.
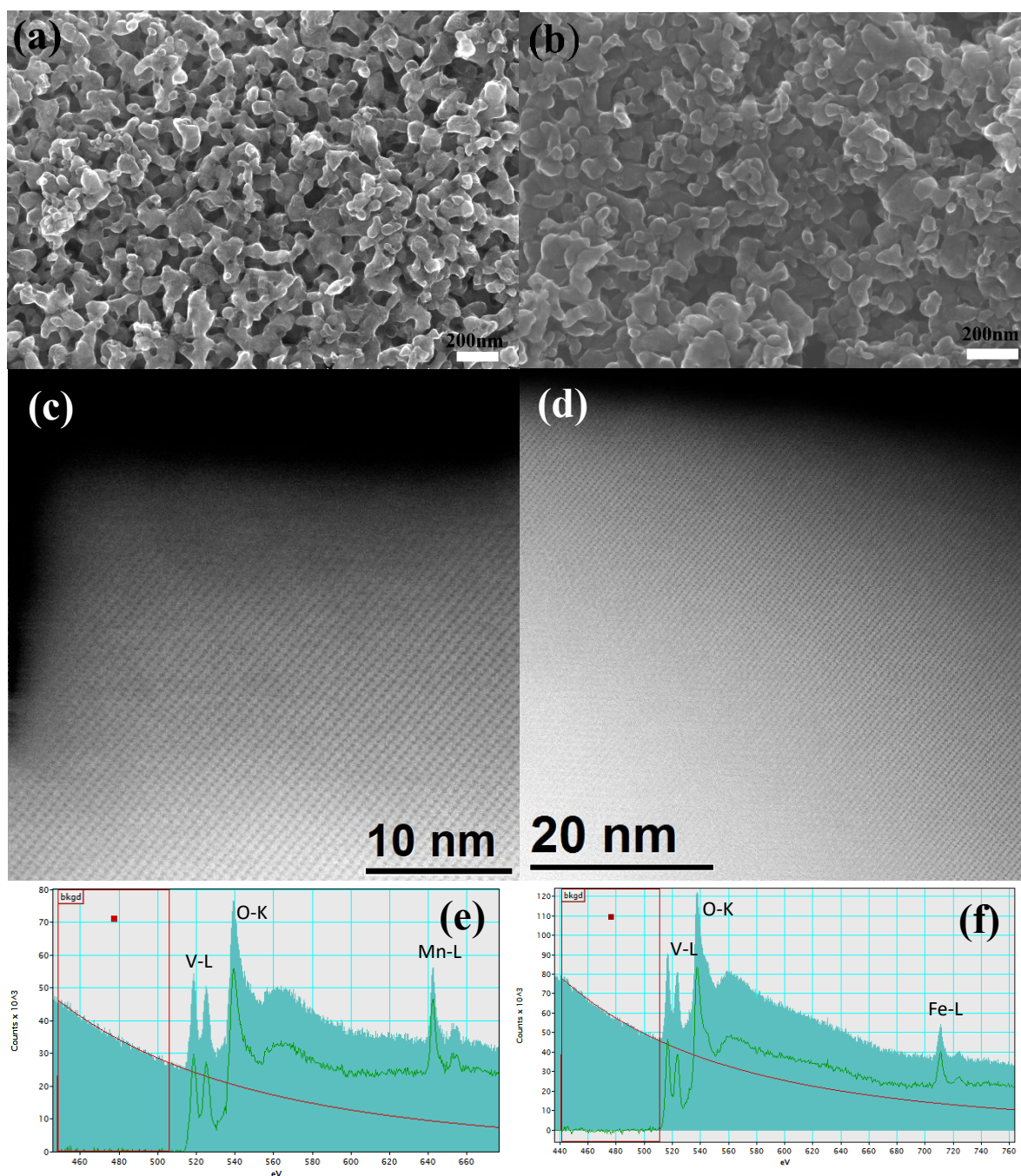
Figure 1. Large scale SEM images of (a) $Na_4MnV(PO_4)_3$ and (b) $Na_3FeV(PO_4)_3$ cathodes. ADF-STEM images and corresponding EEL spectra of $Na_4MnV(PO_4)_3$ in (c) and (e), and $Na_3FeV(PO_4)_3$ in (d) and (f).
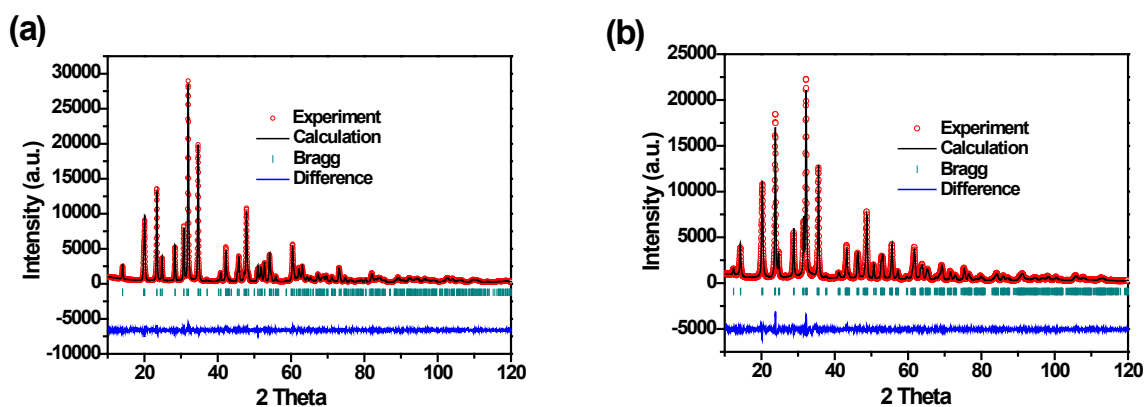
Figure 2. X-ray diffraction pattern and Rietveld refinement of $Na_4MnV(PO_4)_3$ (a) and $Na_3FeV(PO_4)_3$ (b).
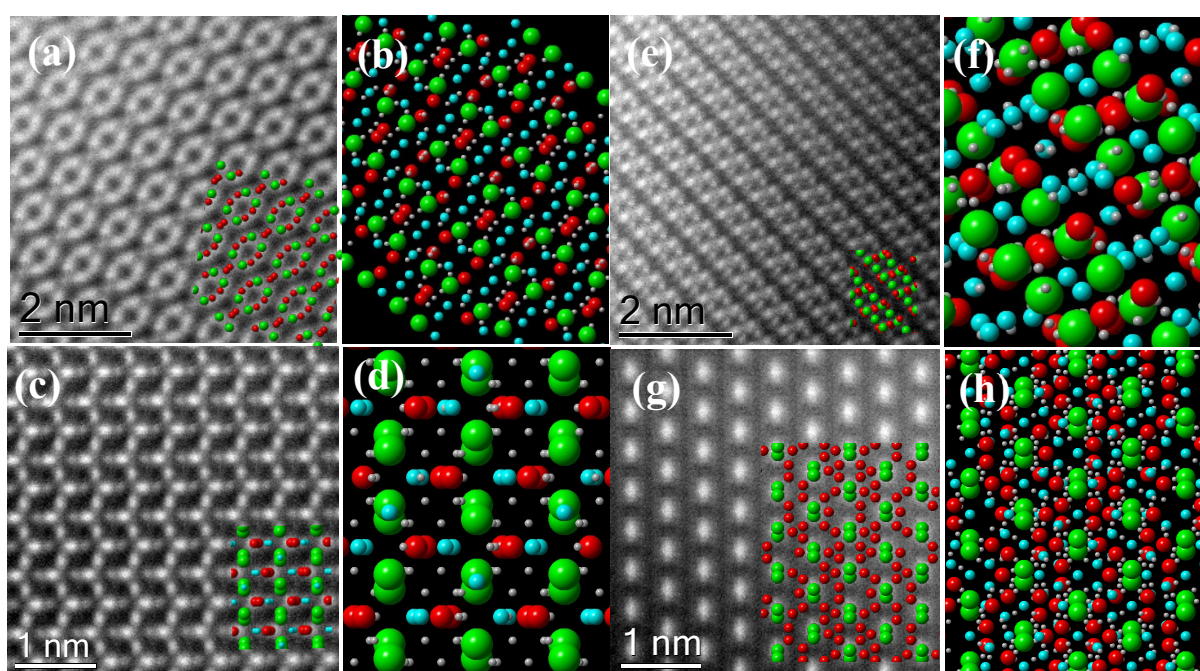
Figure 3. Aberration-corrected ADF-STEM images and crystal structure of $Na_4MnV(PO_4)_3$ viewed from the (a) (b) [-111], (c) (d) [210], (e) (f) [5-21] and (g) (h) [48-1] crystallographic directions. The crystal structure is aligned with the same orientation as the imaged lattice, with Na in cyan, O in grey, P in red and Mn/V in green. The crystal structure without light elements is also overlaid on images, to illustrate the correlation between the image contrast and atom positions. (The same for Figure 4, S2 and S3)
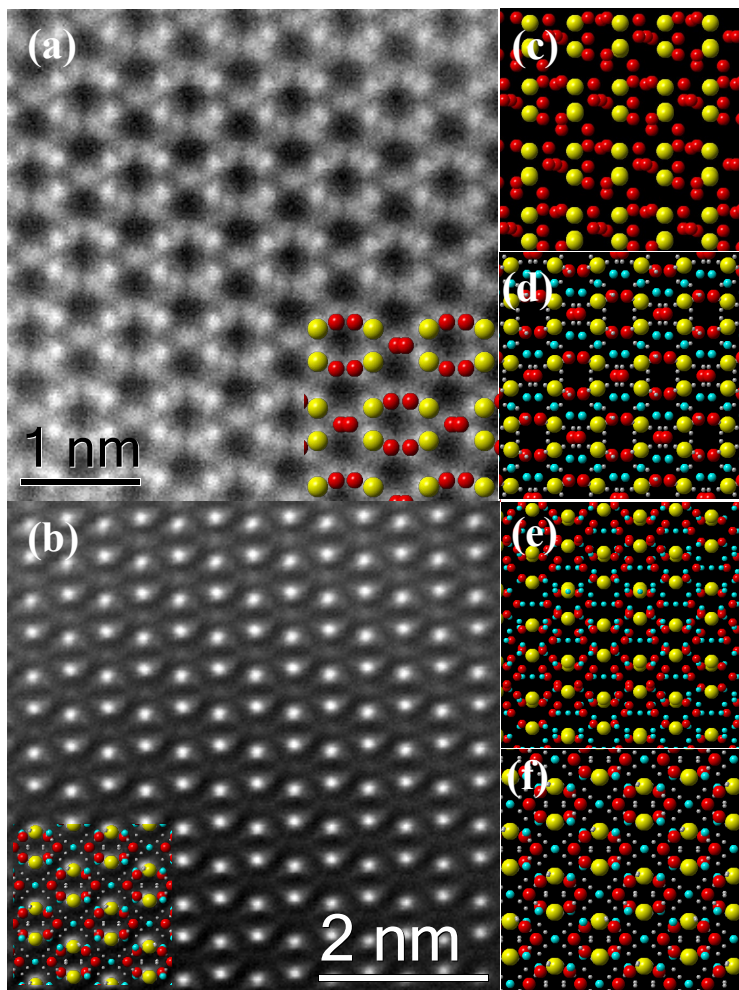
Figure 4. (a), (b) Aberration-corrected ADF-STEM images of $Na_3FeV(PO_4)_3$; and crystal structure viewed from the (c) $Na_3V_2(PO_4)_3$ in [111] (d) $Na_3Fe_2(PO_4)_3$ in [001], (e) $Na_3V_2(PO_4)_3$ in [42-1] (f) $Na_3Fe_2(PO_4)_3$ in [101]. The superimposed atomic array indicating the locations of each atom [Na (green-blue), O (grey), P (red) and Fe/V (yellow)].
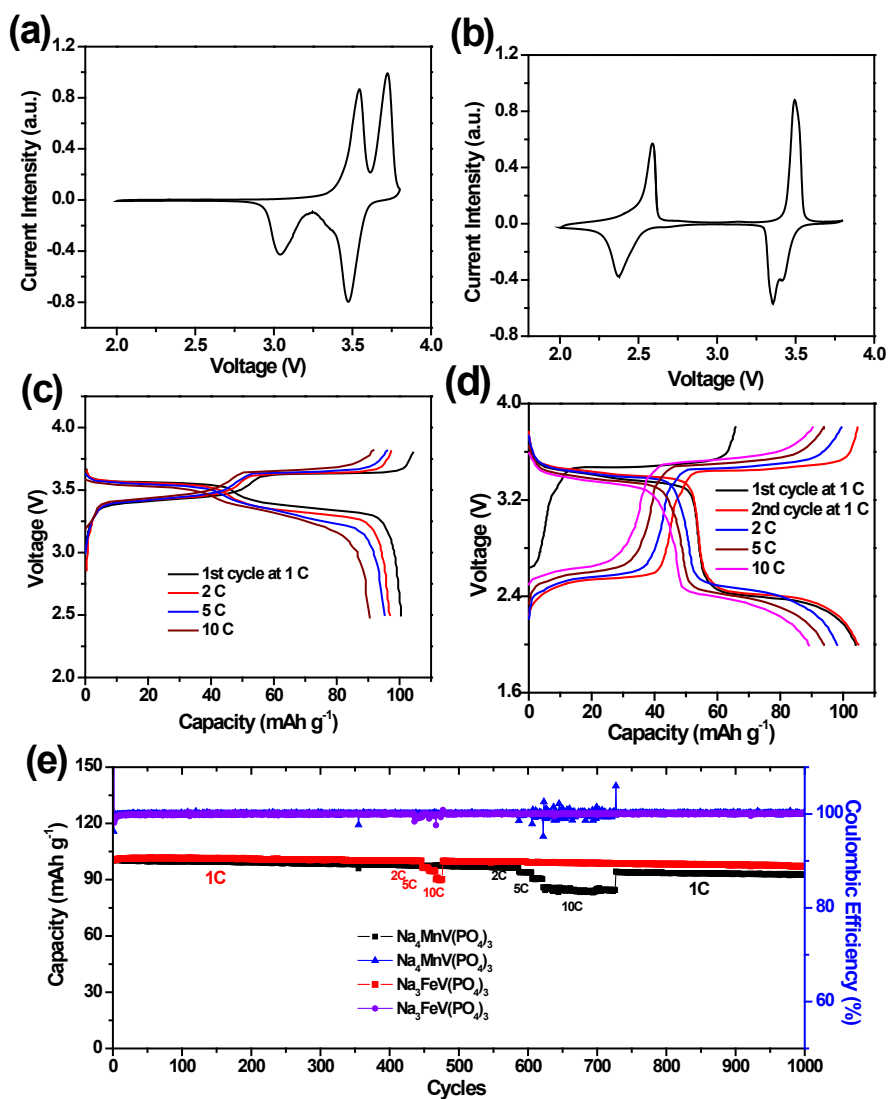
Figure 5. CV curves of Na$_4$MnV(PO$_4$)$_3$ (a) and Na$_3$FeV(PO$_4$)$_3$ (b). Charge and discharge voltage profiles of Na$_4$MnV(PO$_4$)$_3$ (c) and Na$_3$FeV(PO$_4$)$_3$ (d) at different C-rates. (e) Cycling and C-rate performance of Na$_4$MnV(PO$_4$)$_3$ and Na$_3$FeV(PO$_4$)$_3$.
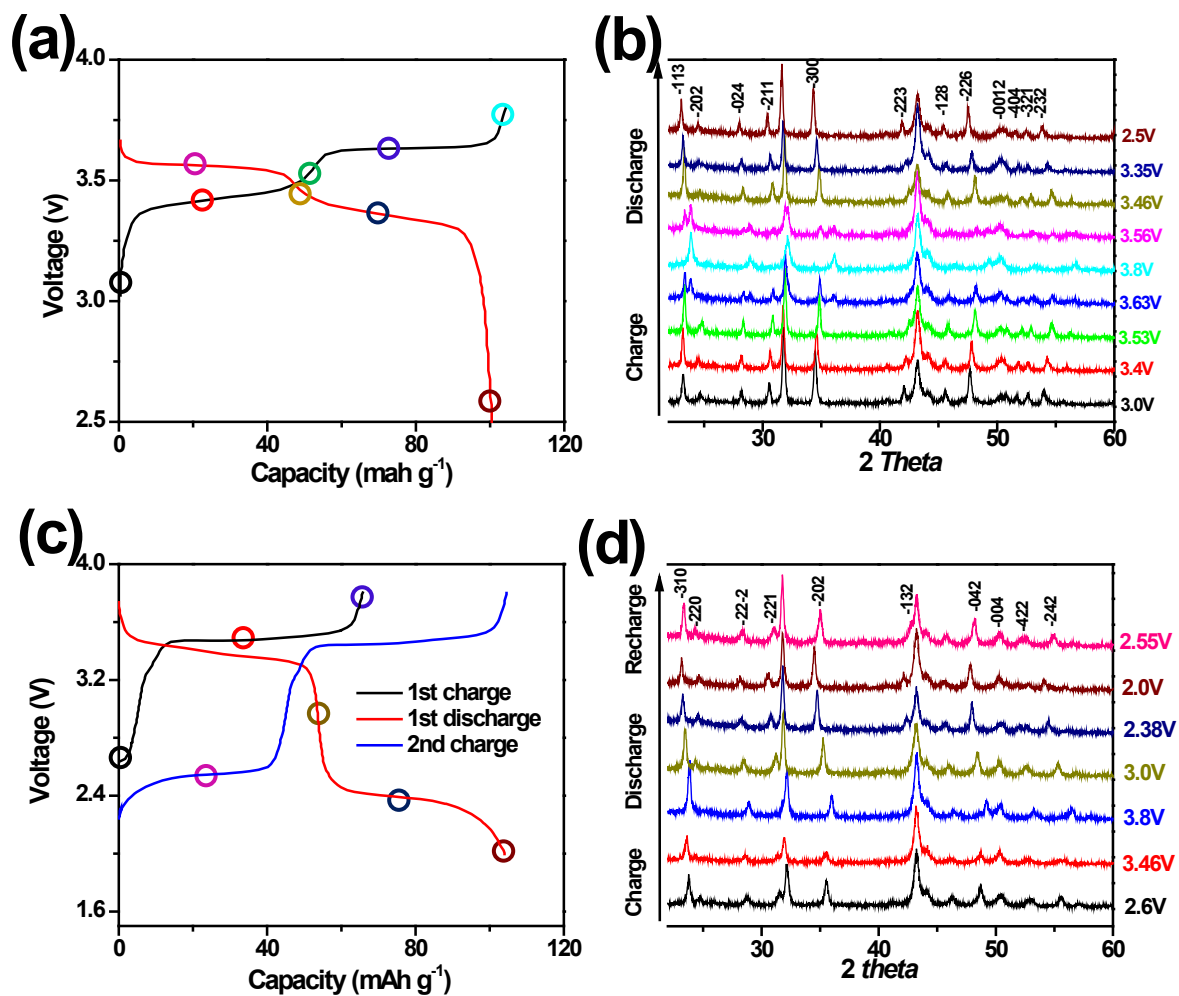
Figure 6. The electrochemical profiles and corresponding *ex-situ* XRD patterns recorded during first charge-discharge of Na$_4$MnV(PO$_4$)$_3$ (a-b) and Na$_3$FeV(PO$_4$)$_3$ (c-d).

A new type of sodium ion battery cathode materials of Na$_x$MV(PO$_4$)$_3$ was prepared, which show superior capacity, high initial efficiency, good durability and rate performance.

Keyword sodium-ion batteries, cathode, NASICON, manganese, phosphates

Weidong Zhou, Yutao Li, Hongcai Gao, Ye Zhu*, Sen Xin, Gengtao Fu, Zhiming Cui, John B. Goodenough*

Lower Cost NASICON-Structured Na$_x$MV(PO$_4$)$_3$ (M=Mn, Fe) Cathodes for Sodium-Ion Batteries

ToC figure ((Please choose one size: 55 mm broad × 50 mm high **or** 110 mm broad × 20 mm high. Please do not use any other dimensions))

Supporting Information

Lower Cost NASICON-Structured Na$_x$MV(PO$_4$)$_3$ (M=Mn, Fe) Cathodes for Sodium-Ion Batteries

Weidong Zhou, Yutao Li, Hongcai Gao, Ye Zhu*, Sen Xin, Gengtao Fu, Zhiming Cui, John B. Goodenough*

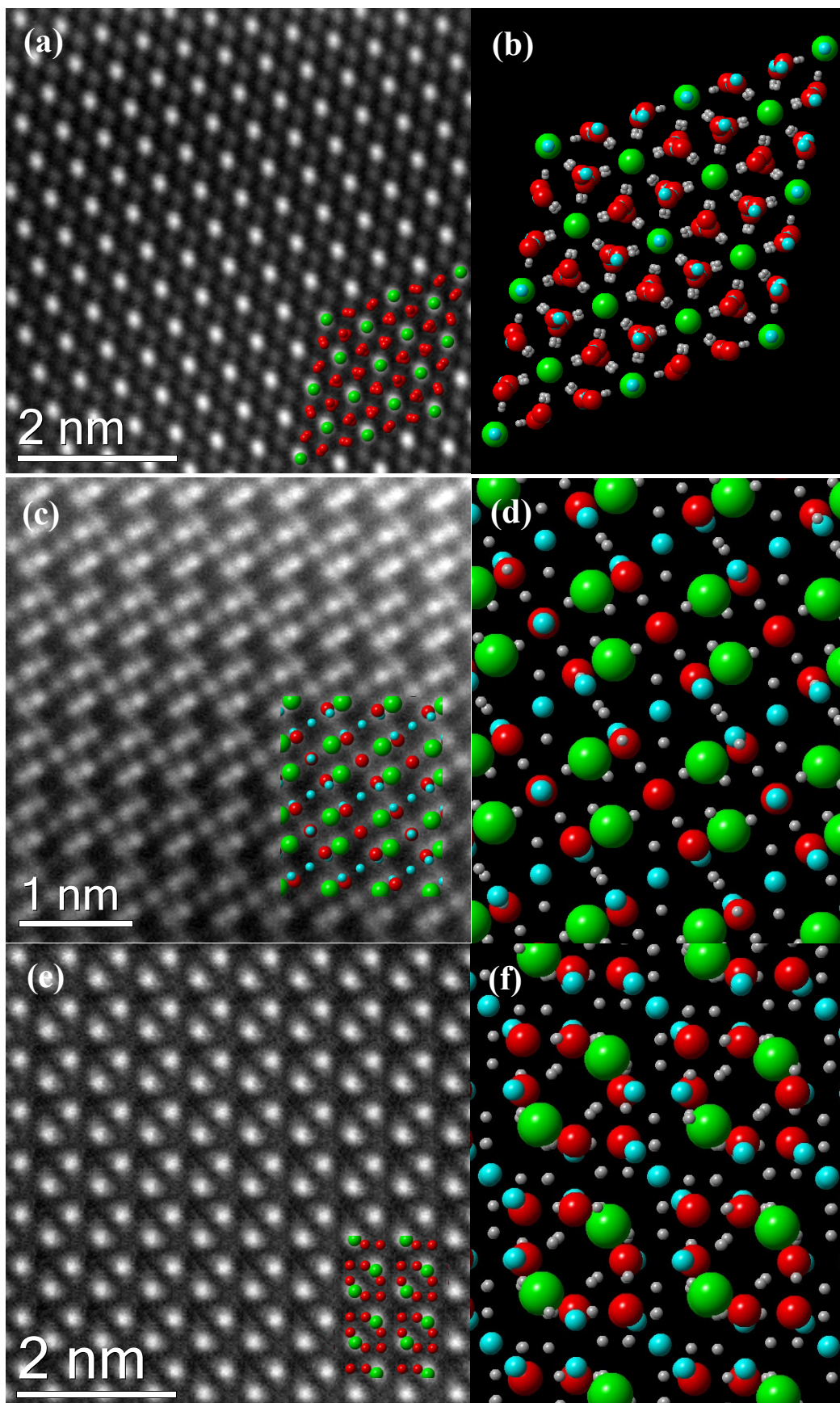**Figure S1.** TGA data of the Na$_4$MnV(PO$_4$)$_3$ and Na$_3$FeV(PO$_4$)$_3$.

Figure S2. Aberration-corrected ADF-STEM images and crystal structure of Na$_4$MnV(PO$_4$)$_3$ viewed from the (a) (b) [001], (c) (d) [110], (e) (f) [42-1] projection. The superimposed atomic array indicates the locations of each atom [Na (green-blue), O (grey), P (red) and Mn/V (green).
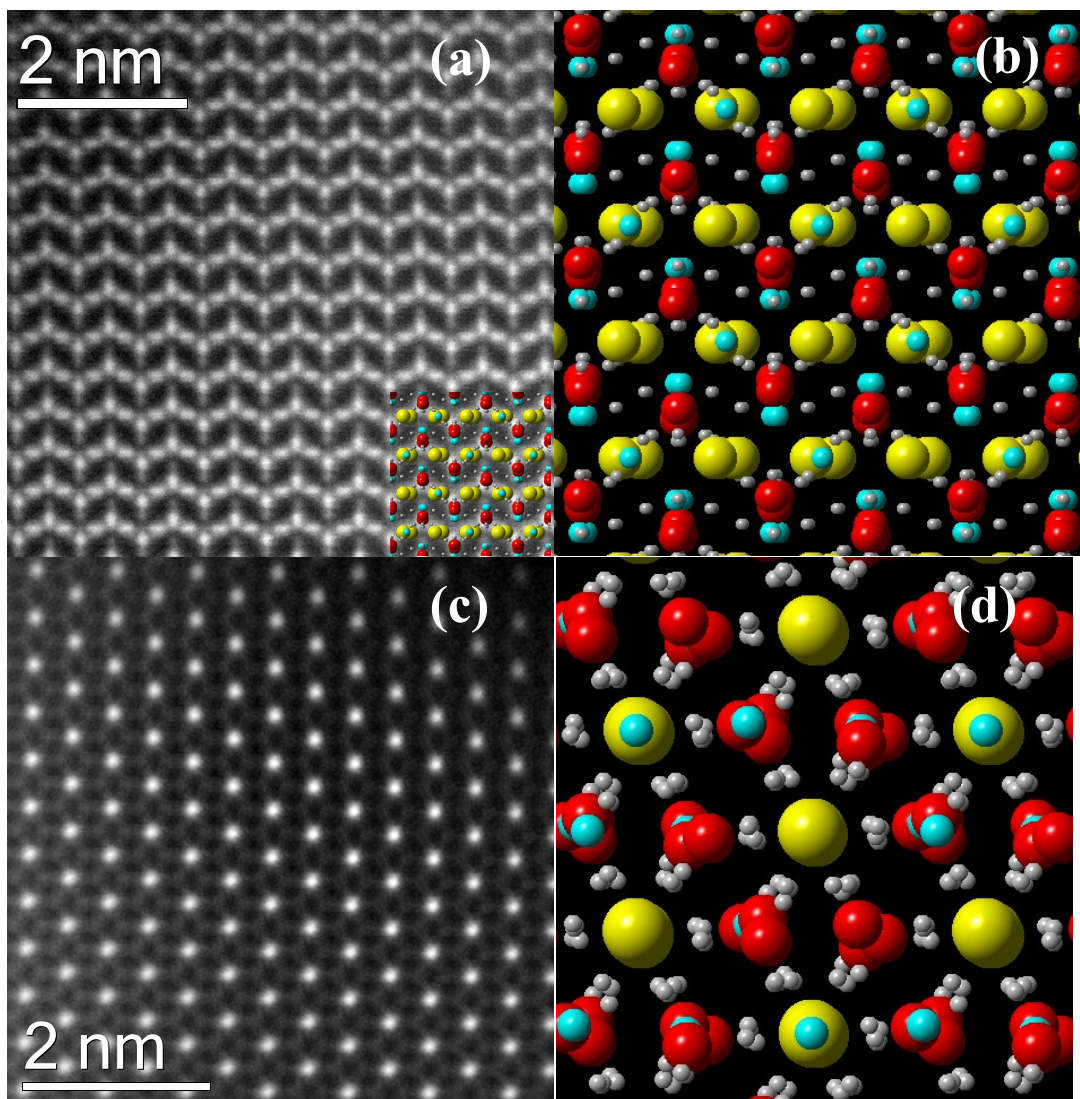
Figure S3. Aberration-corrected ADF-STEM images and crystal structure of $Na_3FeV(PO_4)_3$ viewed from the (a) (b) [201] and (c) (d) [103] crystallographic directions. The superimposed atomic array indicates the locations of each atom [Na (green-blue), O (grey), P (red) and Mn/V (yellow)].
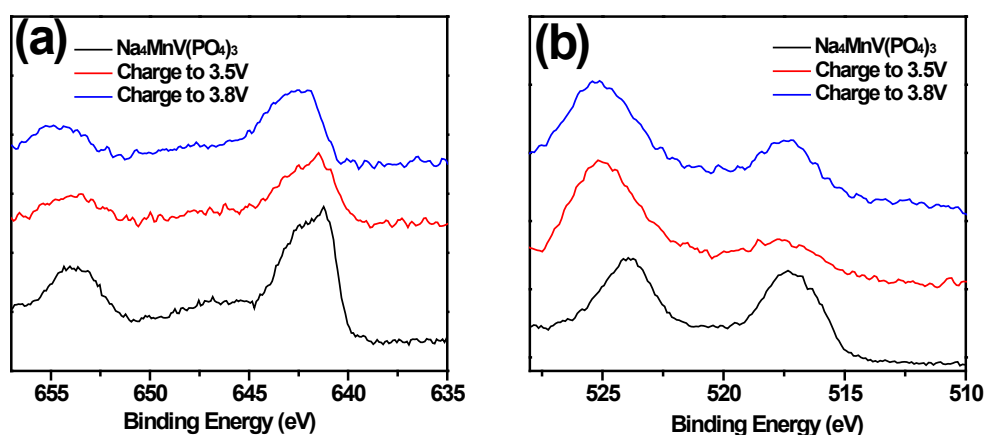

Figure S4. XPS spectra of (a) Mn and (b) V in $Na_4MnV(PO_4)_3$ recorded in different charge voltage.

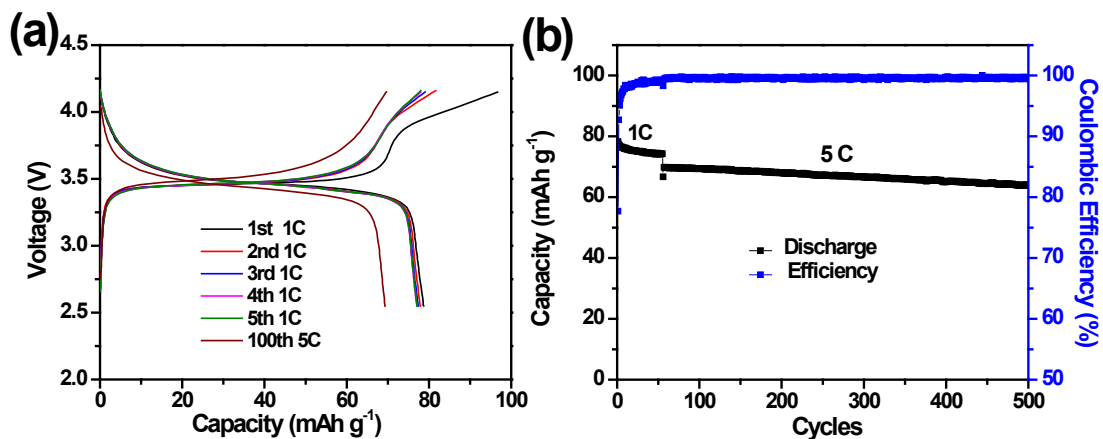**Figure S6.** (a) Charge and discharge voltage profiles, (b) cycling performance of Na4NiV(PO4)3 at different C-rates.
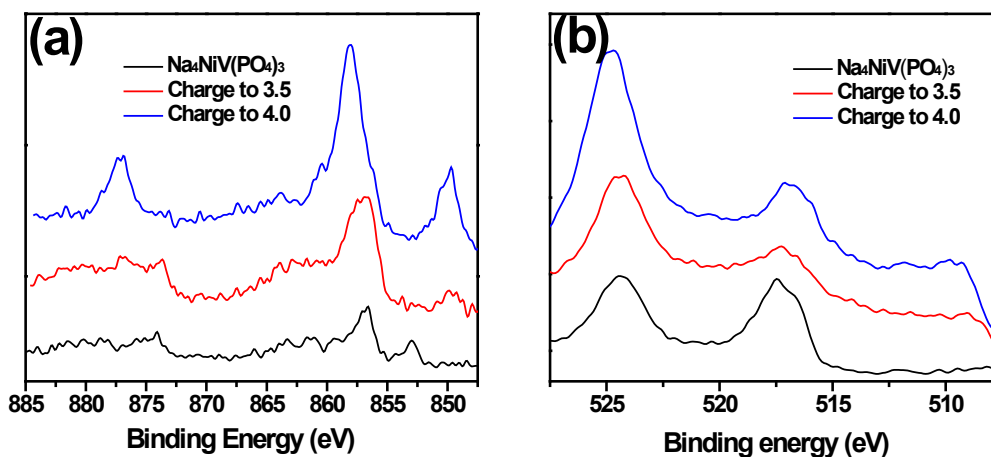

Figure S7. XPS spectra of (a) Ni and (b) V in Na4MnV(PO4)3 recorded in different charge voltage.